Soft Matter

PAPER

View Article Online
View Journal | View Issue

Cite this: *Soft Matter*, 2019, **15**, 7063

Slippery when wet: mobility regimes of confined drops in electrowetting†

Davood Baratian,[a] Élfego Ruiz-Gutiérrez,[b] Frieder Mugele[a] and Rodrigo Ledesma-Aguilar*[b]

The motion of confined droplets in immiscible liquid–liquid systems strongly depends on the intrinsic relative wettability of the liquids on the confining solid material and on the typical speed, which can induce the formation of a lubricating layer of the continuous phase. In electrowetting, which routinely makes use of aqueous drops in ambient non-polar fluids that wet the wall material, electric stresses enter the force balance in addition to capillary and viscous forces and confinement effects. Here, we study the mobility of droplets upon electrowetting actuation in a wedge-shaped channel, and the subsequent relaxation when the electrowetting actuation is removed. We find that the droplets display two different mobility regimes: a fast regime, corresponding to gliding on a thin film of the ambient fluid, and a slow regime, where the film is replaced by direct contact between the droplet and the channel walls. Using a combination of experiments and numerical simulations, we show that the cross-over between these regimes arises from the interplay between the small-scale dynamics of the thin film of ambient fluid and the large-scale motion of the droplet. Our results shed light on the complex dynamics of droplets in non-uniform channels driven by electric actuation, and can thus help the rational design of devices based on electrowetting-driven droplet transport.

Received 3rd June 2019,
Accepted 15th August 2019

DOI: 10.1039/c9sm01107b

rsc.li/soft-matter-journal

Introduction

When a voltage is applied between a droplet of a conducting liquid and a solid electrode, the droplet is observed to spread on the solid. This process, called electrowetting, has received increasing attention in the last decade.[1] This is because, on the one hand, the electrically-driven motion of a droplet on a solid is a model system to understand the interplay between electric, viscous, capillary and wetting forces in fluid dynamics.[2] On the other hand, the ability to control a liquid using electric actuation has enabled or improved many applications,[2,3] including adjustable liquid lenses,[4] electronic displays[5] and droplet microfluidics.[6–8] Most of these applications make use of a second immiscible non-polar liquid that prevents evaporation and typically facilitates droplet actuation by acting as a lubricant.[1]

During electrowetting on a flat surface, a droplet in a completely wetting ambient fluid transitions from a state of no or low initial contact with the solid to a state of partial wetting. The dynamics of this process depends on the competition between the driving electric force, the restoring capillary force, and the dissipative forces arising from the flow within the droplet, the flow within the ambient fluid, and the motion of the three-phase contact line. For sufficiently high spreading speeds, the defending ambient fluid can be entrapped between the droplet and the solid to form a thin film. That film, however, can become unstable and break up into small droplets that remain adhered to the solid[9] leading to an increased contact angle hysteresis and friction.[10] Hence, during electrowetting, a droplet can be found in one of three distinct dynamical regimes: gliding over a thin film of the ambient fluid, advancing over droplets of the ambient fluid, or displacing the ambient fluid completely.

The effect of these dynamical regimes is particularly important for the transport of droplets in channel geometries.[8] First, the mobility of the droplet can be affected by the overall structure of the flow. Second, the static electrowetting configurations of the droplet after transport may depend on whether film break-up has occurred. Third, the relaxation of the droplet upon a variation of the applied electric potential, or its complete removal, is likely to depend on the previous actuation history, leading to hysteresis.[11]

Here, we study the transport of a water droplet immersed in an ambient oil phase as it undergoes a cycle of electrowetting and dewetting within a channel. To induce lateral transport in a preferred direction we use a wedge-shaped channel,[12–18] where the droplet displays inwards motion upon electrowetting,

[a] *Physics of Complex Fluids, MESA+ Institute for Nanotechnology, Department of Science and Technology, University of Twente, The Netherlands*
[b] *Smart Materials and Surfaces Laboratory, Faculty of Engineering and Environment, Northumbria University, Ellison Place, Newcastle upon Tyne NE1 8ST, UK. E-mail: rodrigo.ledesma@northumbria.ac.uk*

† Electronic supplementary information (ESI) available. See DOI: 10.1039/c9sm01107b

and outwards motion when the voltage is removed[19] (dewetting). Experimentally, we study the translation of the droplet upon application and removal of different voltages. During electrowetting, droplets glide on a thin film of the ambient oil phase but suddenly slow down as the droplet touches the surface. During dewetting, droplets initially move slowly, before they detach from the solid and speed up. Numerical simulations based on a newly developed lattice-Boltzmann algorithm[20] reveal that the transition during inwards and outwards motion is in fact controlled by different mechanisms. For inwards motion, where the droplet is driven by electrowetting, the cross-over corresponds to the onset of instability of the entrapped oil film, where the critical speed depends on the applied electrowetting potential, but also on the channel geometry. For outwards motion, corresponding to spontaneous dewetting, the cross-over is controlled by the interplay between the intrinsic timescale of the receding contact line and the timescale of the large-scale motion of the drop.

Experimental setup

Fig. 1a shows the experimental setup used for electrowetting-driven droplet transport in a wedge geometry.[19] Two solid walls are fixed at an angle β relative to the vertical by means of a scaffold. The walls consist of glass plates, on which transparent electrodes of Indium Tin Oxide (ITO) are deposited. A conformal thin layer of Parylene-C, of thickness d_P = 2 μm and dielectric constant ε_P = 3.1, is then added by a chemical vapor polymerization process. This has the purpose of creating a dielectric layer on top of the electrode that provides sufficient resistance against electrical breakdown (up to 100 V_{RMS}). To reduce the contact angle hysteresis on the substrates and to make the surface hydrophobic, a thin layer of thickness ≈100 nm of Teflon AF 1600 (DuPont, USA) is deposited through a dip-coating process and subsequently annealed at 180 °C for 90 min.

The wedge channel is immersed in a quartz cuvette allowing to perform the experiments in an ambient oil environment. We use water droplets (conductivity of 5 mS cm^{-1} – KCl solution) in ambient Bromohexadecane (Merck Millipore, USA) with a density of ρ_{oil} = 0.998 g cm^{-3}, closely matching the density of the salt solution. The oil–water interfacial tension is γ = 43 mN m^{-1}. Therefore, the small difference in density of the two liquids results in a very small Bond number ($B_o = (\rho_{oil} - \rho_{H_2O})gR^2/\gamma \simeq 10^{-4}$) for a typical drop size $R = O$ (1 mm). This minimizes the effect of gravity. Hence, in equilibrium, the free surface of the droplet takes a spherical shape, and intersects the solid with a contact angle θ_Y close to 180°. (Note that contact angles below 10° and above 170° are extremely difficult to measure optically. Absolute values extracted from video snapshots can vary by several degrees depending on illumination settings and exact alignment of the viewing direction, which is difficult in the present wedge geometry. For a detailed discussion see *e.g.* ref. 21.)

To induce electrowetting, an AC voltage with a frequency of 1 kHz is applied between the two planar electrodes forming the wedge using a function generator (Agilent 33220A) together with a voltage amplifier (Trek PZD700A). Throughout the present experiments, drop motion is induced by switching on and off the applied voltage with a step function in time. The droplets in the wedge are imaged with a video camera (uEye). A second camera is used to monitor the drop-substrate area through the transparent substrates. We use an in-house image analysis script (written in Matlab) to extract the profile of the droplets and their position relative to the walls of the channel.

Results

Fig. 1b shows time-lapse images of the motion of a droplet of volume V = 12 μl in a wedge of opening angle β = 12.5° during a cycle consisting of electrowetting actuation followed by spontaneous dewetting. Initially, the droplet is positioned between the two solid plates forming the wedge. Its equilibrium shape corresponds to a sphere, with an apparent contact angle θ_Y ≈180°. Applying a voltage, U = 100 V, leads to an abrupt reduction of the apparent contact angle to a new equilibrium value $\theta_e \approx 123° \pm 2.32°$. As a consequence of the reduced contact angle, the drop moves towards the apex of the wedge, until it reaches a new equilibrium configuration which corresponds to a truncated sphere with a voltage-dependent apparent contact angle $\theta_e(U)$. Removing the

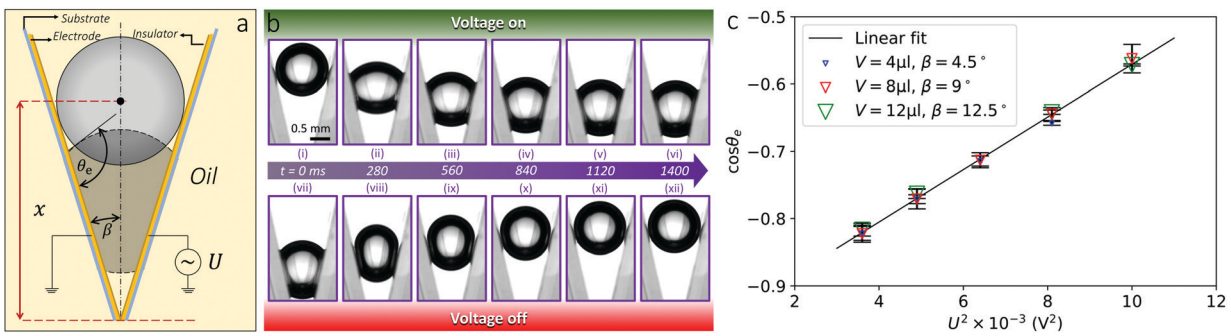

Fig. 1 Droplet transport in a wedge channel driven by electrowetting (a) schematics of the static drop profile with/without applied voltage (dashed/solid contour). The position of the droplet, $x(t)$, is defined as the distance between the center of the droplet from the apex of the wedge. (b) time-lapse images of a drop of volume V = 12 μl in a wedge of opening angle β = 12.5° driven by an applied voltage U = 100 V (top row) and dewetting upon removal of the applied voltage (bottom row). (c) Dependence of the apparent contact angle with the applied voltage. The straight line corresponds to a fit to the Young–Lippmann equation (see text).

applied voltage leads to a sudden increase in the contact angle and a spontaneous translation away from the apex towards the wider region of the wedge.

Because of the geometry of the wedge and the conservation of the volume of the liquid, the equilibrium radius of the droplet, $R_e = [6V/\pi(\cos 3\theta_e - 9\cos\theta_e)]^{1/3}$, and the position of its center relative to the apex of the wedge, $x_e = -\cos\theta_e R_e/\sin\beta$, are completely determined by the drop volume V, the opening angle β of the wedge, and the voltage-dependent apparent contact angle, θ_e.[19] This imposes practical limitations on the range of parameters accessible in the experiments. For the range of voltages considered in this study (60–100 V; s.d. 0.09 V), we studied three combinations of the droplet volume and the wedge angle, namely: 4 μl ± 0.16 μl and 4.5° ± 0.21°, 8 μl ± 0.16 μl and 9° ± 0.21°, and 12 μl ± 0.16 μl and 12.5° ± 0.21°. These choices ensure that the droplets travel over distances that are feasible for studying their motion, of at least 1 mm and below the length of the wedge walls.

From the classical theory of electrowetting, we expect that the apparent contact angle varies with the applied voltage obeying the Young–Lippmann's equation,[1]

$$\cos\theta_e = \cos\theta_Y + \eta, \quad (1)$$

where $\eta = cU^2/2\gamma$ is the electrowetting number and c is the capacitance per unit area of the dielectric gap between the conducting droplet and the solid electrode. Indeed, for the range of parameters considered in our experiments, a plot of $\cos\theta_e$ *vs.* U^2 is well described by a linear relation (see Fig. 1c). Furthermore, the figure shows the collapse of the data onto a single curve; this implies that θ_e is independent of the droplet volume and of the angle of the wedge and further validates eqn (1). In our experiments the dielectric configuration results from a layer of Paralyne-C, a Teflon layer, and a layer of bromohexadecane. From the data, we measured the corresponding capacitance per unit area using a linear fit, yielding $c = 3.3616 \times 10^{-6} \pm 6 \times 10^{-8}$ F m^{-2}. In the following, we will use this value to compute the electrowetting number.

From the time-lapse images in Fig. 1, it is clear that the morphology of the droplet during inwards and outwards displacements is very different. Upon moving inward, Fig. 1b(i)–(vi), the apparent contact angle quickly decreases close to the equilibrium value θ_e corresponding to the applied voltage U as the drop gradually relaxes towards its final position. Throughout this process, there seems to be a finite contact area between the drop and the substrate. Upon dewetting, on the other hand, Fig. 1b(vii)–(xii), there is a strong asymmetry between the advancing and the receding side; the contact angle stays close to $\theta_e(U)$ on the receding side (although U has been removed) and $\theta_e \approx \theta_Y$ on the advancing side. To quantify the droplet dynamics, we plot the instantaneous position of the drop center $x(t)$ with respect to the apex of the wedge channel. Fig. 2a and b show typical $x(t)$ curves for inward and outward translation. At first sight, the motion appears to follow an exponential relaxation from the initial position x_0 to the final position x_e. However, plotting the relative position $\tilde{x} = (x(t) - x_c)/(x_0 - x_c)$ on a semi-logarithmic scale reveals that the motion is characterized by two distinct exponential relaxation processes. The inward motion is characterized by a fast first relaxation with a time constant $\tau_1^{(in)}$, followed by a slower second relaxation regime with a time constant $\tau_2^{(in)} > \tau_1^{(in)}$ after some cross-over time t^*. During the outward relaxation, however, the system displays a rather peculiar behavior: first there is a slow and later a faster relaxation with time constants $\tau_1^{(out)}$ and $\tau_2^{(out)}$ where $\tau_1^{(out)} > \tau_2^{(out)}$.

This phenomenology was observed for the entire parameter range studied with various droplet volumes (4–12 μl), wedge angles (4.5°–12.5°), and applied voltages (60–100 V). Overall, the strength of the driving force, either during electrowetting or spontaneous dewetting, can be characterized by measuring the total lateral displacement of the droplet, $x_0 - x_e$ (note that x_0 and x_e always refer to the initial and final equilibrium droplet positions, regardless of the direction of motion). As shown in Fig. 3a, for fixed volume and wedge angle, $\tau_1^{(in)}$ remains approximately constant with varying driving force while $\tau_2^{(in)}$ shows no obvious systematic trend. This situation changes for outwards

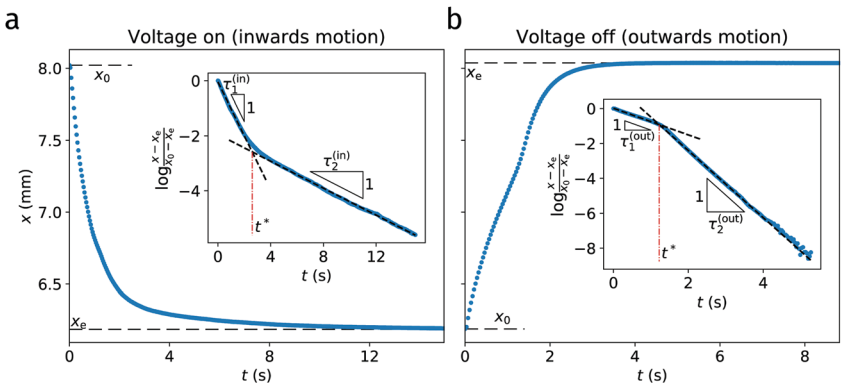

Fig. 2 Time evolution of drop position during inwards (a) and outwards (b) motion. The data represents the position of a drop of V = 8 μl in a wedge with an opening angle of β = 9° under application/removal of a voltage U = 100 V. The initial and final positions during each step of the cycle are indicated by the dashed lines. Insets: Semi-log plots of the normalized displacement from the equilibrium position. Two distinct relaxation regimes for the droplet can be identified during each step, indicated by the triangles; the corresponding cross-over time, t^*, is indicated by the vertical dot-dashed lines.

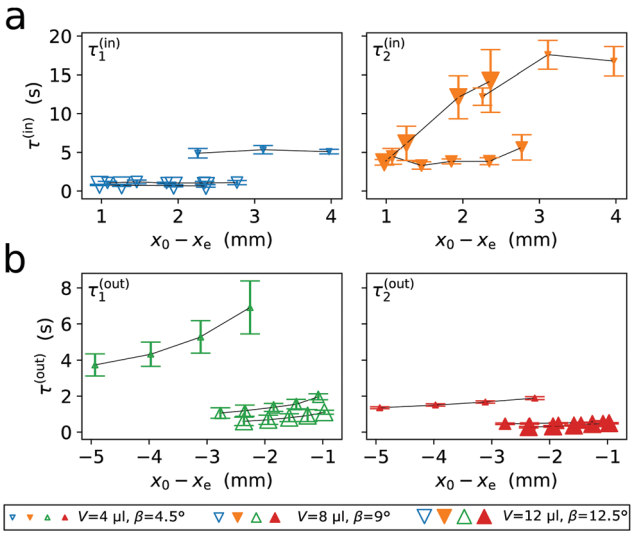

Fig. 3 Relaxation time constants *vs.* droplet displacement for variable drop size and wedge angle, increasing with increasing symbol size (see legend). (a) Inward relaxation (voltage on); open and closed symbols correspond the relaxation times, $\tau_1^{(in)}$ and $\tau_2^{(in)}$. (b) Outward relaxation (voltage off – with voltage-dependent initial position x_0); open and closed symbols correspond the relaxation times, $\tau_1^{(out)}$ and $\tau_2^{(out)}$.

motion, where both relaxation constants $\tau_1^{(out)}$ and $\tau_2^{(out)}$ increase with decreasing deviation from equilibrium (Fig. 3b).

Discussion

Let us first discuss the driving and dissipative forces acting on the droplet during its motion within the wedge channel. Starting with the driving forces, we first consider the Helmholtz free surface energy of the drop, F, as a function of its position, x,

$$F(x;\cos\theta_e) = \gamma(A - A_{sl}\cos\theta_e). \quad (2)$$

Here, A is the free surface area of the drop (*i.e.* the oil–water interfacial area) and A_{sl} is the drop-substrate interfacial area. The dependence $F(x)$ can be found by constrained numerical minimization, or modeled by analytical approximation, as discussed by Ruiz-Gutiérrez *et al.*[22] For a given contact angle, F has a minimum at a position x_e, where the droplet shape is a truncated sphere with contact angle θ_e. Upon displacing the drop inward or outward from x_e, the surface energy increases, as shown in Fig. 4a. In the experiments, θ_e decreases by increasing the applied voltage, leading to a reduction of the surface energy and a corresponding decrease in the equilibrium position, x_e. Because the change in equilibrium contact angle occurs in a relatively short timescale, the droplet switches from one energy landscape, $F(x_0;\cos\theta_Y)$, to another, $F(x_0;\cos\theta_e(U))$, where $x_0 > x_e$ (see vertical arrows in Fig. 4a). Hence, the droplet moves inwards driven by the restoring capillary force, which corresponds to the local gradient of the curve $F(x;\cos\theta_e)$. Similarly to the situation of electrowetting-induced drop jumping[23] the amount of energy stored in the non-equilibrium configuration of the drop is very different for the on-switching as compared to the off-switching process. Because of the asymmetry of $F(x)$, the relaxation following the on-switch process is much more gradual with an almost constant gradient, $-dF/dx$, whereas the outward relaxation upon switching off the voltage involves much steeper energy gradients due to the geometry of the wedge (compare the slope of the energy landscapes for regions labeled "voltage on" and "voltage off" in Fig. 4a). This is consistent with the weak dependence of the relaxation time on the applied voltage observed in Fig. 3a (on-switch) and the much more pronounced voltage-dependence of the off-switching process in Fig. 3b. In particular, the strong curvature of the topmost energy curve in Fig. 4a (zero voltage) for small x implies a very strong driving force upon releasing drops that were initially pulled deep into the wedge by a high voltage.

Close to equilibrium and for small wedge angles, the restoring force can be modelled as $-dF/dx \approx -k(x - x_e)$, where $k \sim \gamma\beta^2$. To model the opposing dissipation forces, Ruiz-Gutiérrez *et al.*[22] considered the friction caused by the flow within the bulk of the droplet, the flow within the vicinity of the contact line, and the motion of the contact line itself. This leads to a friction force $-\nu dx/dt$, with a friction coefficient $\nu \sim \mu V^{1/3}$. The balance

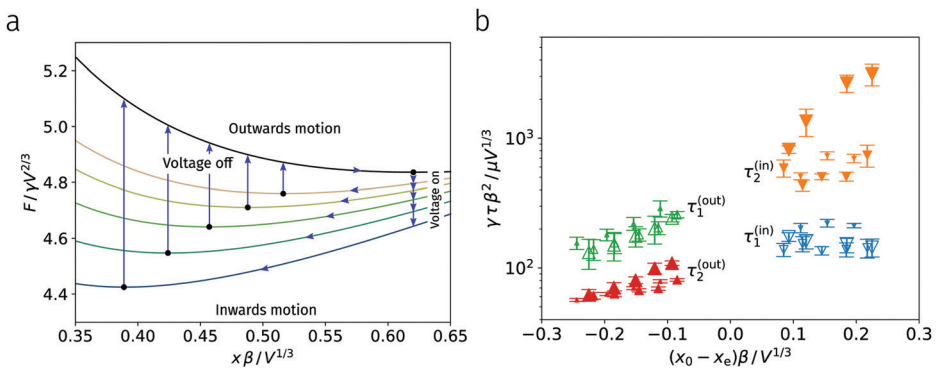

Fig. 4 (a) Surface energy of droplets perturbed from their equilibrium position for different equilibrium contact angles. From bottom to top, the curves correspond to θ_e = 125°, 130°, 135°, 140°, 145° and 180°. During sudden electrowetting actuation, the apparent contact angle is reduced to $\theta_e(U)$; a droplet follows the path indicated by the arrows to find a new equilibrium position in the energy landscape, which is closer to the apex of the wedge for lower θ_e (filled circles) (b) Reduced relaxation times as a function of the initial displacement from equilibrium. The symbols correspond to the same experimental parameters reported in Fig. 3.

between these forces then leads to an exponential approach to equilibrium, with a time constant $\tau = \nu/k \propto \mu V^{1/3}/\gamma\beta^2$. Fig. 4b shows the measured relaxation times from Fig. 3 rescaled by the characteristic time, $\mu V^{1/3}/\gamma\beta^2$, as a function of the displacement from the droplet's equilibrium position (also rescaled by the length $V^{1/3}/\beta$ following ref. 19 and 22). Rescaling to these non-dimensional parameters collapses the data for variable volumes and wedge angles (except for the largest volume and wedge angle for $\tau_2^{(\mathrm{in})}$), suggesting that the theory of ref. 19 and 22 captures the overall scaling of the driving and dissipative forces. However, unlike the experiments in ref. 22, there is clearly no single and universal curve that describes both inward and outward relaxation. In particular, the single friction force of ref. 22 does not capture the succession of fast and slow relaxation processes as shown in Fig. 2 and 3.

To rationalize the order of the fast and slow relaxation processes, we note that there is initially little contact between the droplet and the substrate as the voltage is applied (see first snapshot in Fig. 1b); this suggests that the faster initial motion with $\tau_1^{(\mathrm{in})}$ is facilitated by the entrapment of a thick film of ambient oil, which allows the droplet to glide past the solid. As the droplet moves into the wedge, the sudden change to a slower motion suggests the onset of contact between the droplet and the wall, and consequently, the formation of a contact line that slows down the interface. On the other hand, for outwards displacements the droplet is initially in contact with the walls, and its motion is limited by the presence of a contact line. The subsequent abrupt decrease in the relaxation time ($\tau_1^{(\mathrm{out})} > \tau_2^{(\mathrm{out})}$) indicates a detachment from the solid and a re-entrant entrapment of a lubricating oil film.

This qualitative picture is supported by images of the interface between the drop and one of the two side walls of the wedge through the transparent substrate (Fig. 5). Fig. 5a shows time-lapse images of a 12 μl droplet upon electrowetting actuation at U = 100 V. The yellow boxes indicate the blow-up regions presented in Fig. 5b–g. As anticipated, and based on the side view images, the droplet shows no obvious contact with the wall before the voltage is applied (Fig. 5b). Upon electrowetting actuation, the droplet is forced against the wall and entraps a film of oil that eventually ruptures to form droplets (Fig. 5c). These droplets of oil are left adhered to the wall. As the drop moves inwards, the trailing edge of the water drop comes close to these (rather large) early stage oil droplets (Fig. 5d). In addition, newly formed oil droplets appear and spread across the macroscopic (water) drop-substrate interface forming an advancing front, which trails behind the leading droplet's edge (red dashed line in Fig. 5e and f). Finally, as the droplet reaches an equilibrium position, this front gradually catches up with the leading edge of the droplet (Fig. 5g). These substrate-view images thus confirm the anticipated existence and a rather complex temporal evolution of a lubrication layer that eventually breaks up into small oil droplets underneath the macroscopic water drop. The latter behavior is not unexpected. In the context of electrowetting-induced spreading of a sessile drop on a flat surface in ambient oil Staicu and Mugele[9] indeed demonstrated the same two phenomena: (i) the advancing macroscopic

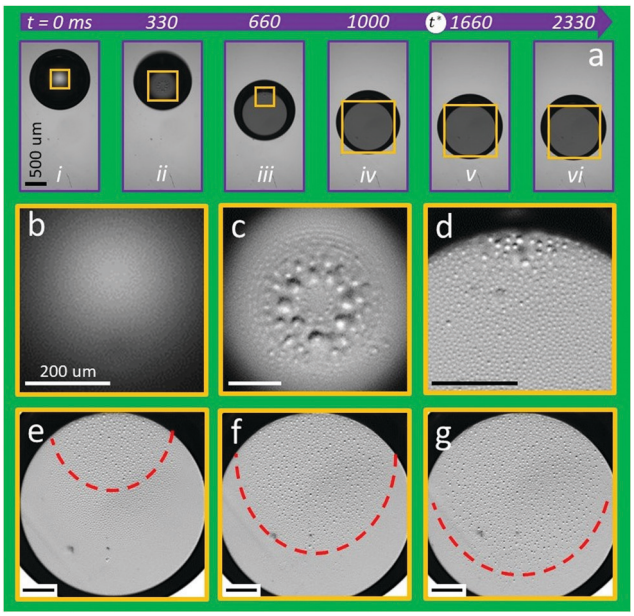

Fig. 5 Side view images of droplet (V = 12 μl) during its translation in the wedge (β = 12.5°) under electrowetting (a) (i)–(viii)). (b)–(g) are zoomed-in images of (a) depicted with yellow frames. (b) Drop at its initial position. (c) formation of oil droplets upon applying electrowetting. (d) Residual large oil droplets which were formed in (c), adjacent to newly-formed smaller droplets. (e)–(g) Growth of the lubricant oil instability, and expansion of the area covered by the dewetted oil droplets beneath the droplet. The scale bar in (a) is 500 μm and in (b)–(g) is 200 μm.

edge of the drop dynamically entraps a layer of ambient oil to form an electrowetting-controlled Landau–Levich (or Bretherton) film. For the sessile drop case, the thickness of the entrapped film scales a $h \sim Ca^{2/3}/U^{4/3}$, where $Ca = \mu_a v/\gamma$ is the capillary number and v the speed of the leading edge of the drop. The thickness of the entrapped oil layer is thus governed by the balance of capillary and viscous forces. (ii) Once entrapped, this oil film is subject to a Maxwell stress acting on the oil–water interface. The competition between Maxwell stress and surface tension then leads to linear instability of the film and break-up into small droplets beyond a critical wavelength that decreases with increasing voltage. The drop size seen in the final state reflects the fastest growing unstable mode, which scales (for relevant conditions) as $\lambda_{\mathrm{m}} \propto \left(1+\tilde{h}\right)^{\frac{3}{2}} \Big/ U$, as discussed in ref. 1 and 9. Here $\tilde{h} = h\varepsilon_{\mathrm{d}}/d\varepsilon_{\mathrm{oil}}$ is the normalized dielectric thickness of the oil film (d, ε_{d}: thickness and dielectric constant of dielectric layer). At the same time, the associated characteristic growth rate increases with decreasing film thickness as $\Gamma_{\mathrm{m}} \propto h^3U^4$ for $\tilde{h} \ll 1$ because of the diverging hydraulic resistance of the thin oil film.

The images shown in Fig. 5 depict the same qualitative scenario. Upon turning on the voltage, the water drop initially spreads and then starts to translate at a rather high speed leading to the entrapment of a thick oil layer, consistent with the observation of rather large oil drops in Fig. 5c. As the drop slows down at later stages upon approaching equilibrium, Ca and hence the thickness of the entrapped oil film decreases,

corroborated by the smaller size of the drops seen in the subsequent panels of Fig. 5. Since Γ_m decreases as h^3, the instability lags behind the moving contact line and only gradually expands over the entire (water) drop-substrate interface as the drop finally approaches its new equilibrium position (Fig. 5d–g). Overall, we associate the transition from fast to slow relaxation with the collapse of the lubricating oil film as the friction on the drop increases with decreasing drop speed and hence lubrication film thickness.

Upon removing the applied voltage, the drop initially experiences a very high friction due to the absence of a lubrication layer. As it gradually relaxes, the macroscopic leading edge of the drop entraps a thick oil layer which then lubricates the drop. (We avoid the word contact line to emphasize that there is no three-phase contact.) As soon as the trailing edge drop is completely ''peeled off'' from the surface, the entire drop-substrate interface is lubricated again. Hence, the drop is fully detached from the substrate and relaxes towards the new final position.

Based on the experimental observations, we attribute the cross-over between the different high and low mobility regimes to the transition between film entrapment and breakup of the lubricating oil film. Yet, it does not become fully obvious from these observations how to pinpoint exactly the moments of transition between the different regimes. Therefore, we carried out numerical simulations of the coupled hydrodynamics and electrostatics equations of motion. We used a two-dimensional diffuse-interface model which we integrated using a lattice-Boltzmann algorithm (see ref. 20 for details of the validation of the method and the ESI† for a list of simulation parameters). The electrolytic solution is modeled as a perfect conductor whereas the oil phase is modeled as a perfect dielectric. The viscosity of the oil phase is set to 4 times the viscosity of the electrolytic solution. The thin dielectric layer separating the liquids from the electrodes is modeled as a solid layer of uniform electric permittivity. The frame of reference is fixed to the leading edge of the droplet, which is kept at the midpoint of the channel, by adjusting the flow rate at the ends of the simulation box. The Young's angle between the fluids is controlled by adding a surface energy term, leading to $\theta_Y = 144^\circ$. This choice ensures numerical stability in the simulations, but it also allows us to explore the full transition between film gliding and breakup for approximately the same range in the electrowetting number studied in the experiments.

Fig. 6a shows four representative examples of the configuration of the liquid–liquid interface as its speed, v, is varied. For sufficiently large v, a stable oil film of uniform thickness, h, is entrapped between the droplet and the solid wall. Decreasing the interface speed leads to a reduction of the thickness of the film, which develops perturbations that grow as they travel downstream. These perturbations have a destabilizing effect on the film, which eventually breaks up into small drops as the conducting fluid reaches the solid and creates a contact line.[9,20] Once a contact line is formed, there is a range of interface speeds where the contact line lags behind the rest of the interface, leading to the deposition of droplets. Finally, at sufficiently low speeds, the speed of the contact line matches that of the rest of the interface, and the motion proceeds as dynamic wetting. The same transition from film-entrapment to dynamic wetting as the front speed is reduced occurs for different values of the applied potential, albeit at a critical speed, v^*, that increases with U.

Fig. 6b shows the corresponding ''phase diagram'', which we report in terms of the capillary number, $Ca = \mu v/\gamma$, and the electrowetting number, η. Each point in the figure corresponds to a different simulation, whose color indicates the minimum local thickness of the film. The trajectory depicted in the figure can be used to understand the evolution of the film during the inwards motion of the droplet observed in the experiments. Initially, when the voltage is switched on, the droplet moves at a relatively high speed. Hence, a Landau–Levich film is entrapped, leading to a relatively high mobility. The droplet, however, progressively slows down as it moves into the wedge, and so the film becomes thinner, until the onset of film breakup is crossed. The resulting formation of droplets leads to a higher friction force due to the presence of multiple contact lines, slowing the droplet further.

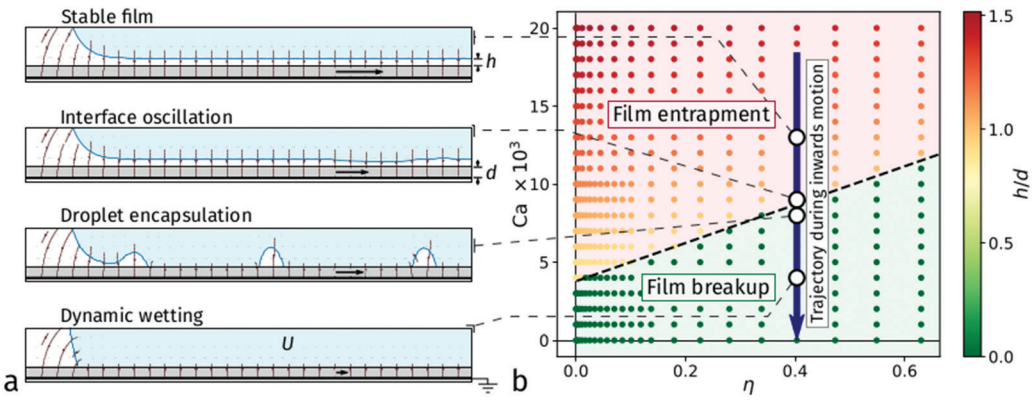

Fig. 6 Lattice–Boltzmann simulations. (a) Spreading of a conducting fluid (light blue) by electrowetting on a solid dielectric (grey) of thickness d. At low speeds, a stable film oil of thickness h is entrapped between the droplet and the solid. As the speed is reduced the film develops oscillations driven by the electric field, which eventually develop as droplets. For sufficiently low speeds the film completely disappears and a stable contact line advances on the solid. The vertical axis has been expanded 2× for visibility. The direction of the electric field is represented by the field lines. (b) Film-entrapment and film breakup regimes as a function of the capillary and electrowetting numbers. The configurations reported in (a) are indicated by the empty circles.

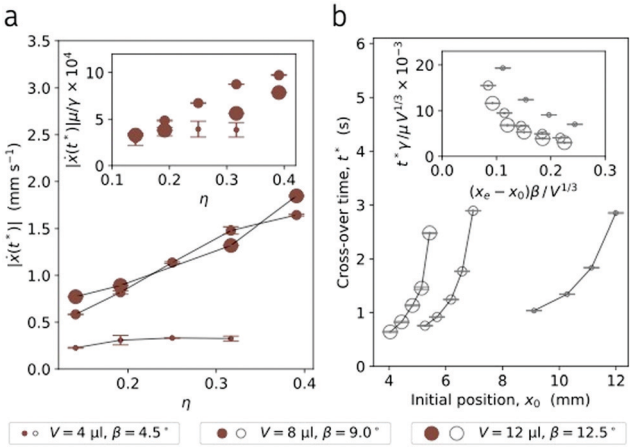

Fig. 7 Cross-over during inwards and outwards motion. (a) Interface speed at the cross-over time as a function of the electrowetting number. (b) Cross-over time during outwards motion as a function of the initial position of the droplet. Inset: Data collapse in terms of the timescale of motion of the contact line and the dimensionless deformation of the interface shape.

Fig. 7a shows experimental measurements of the speed of the droplet at the crossover time, $\dot{x}(t^*)$, as a function of the electrowetting number. The data show an increasing critical speed with increasing η, as expected from the simulations. The data also show a decrease in the critical speed for the smallest droplet volume and wedge angle considered in the experiments. This effect can be explained in terms of the geometry of the system: a smaller droplet has to travel a relatively longer distance into the wedge in order to create the equivalent thin-film area underneath it. Hence, smaller droplets are able to travel longer distances into narrow wedges before the ambient film destabilizes, leading to lower critical speeds.

The inset in Fig. 7a shows the experimental data in terms of the capillary number. The transition occurs for smaller Ca values than observed in the simulations. This is likely due to the lower surface wettability in the experiments ($\theta_Y \approx 180^\circ$), which can ensure a stable film of relatively low thickness.

The numerical simulations also offer insights into the mechanism governing the change in mobility during outwards motion. Upon removal of the applied voltage, the droplet is pushed outwards due to the large-scale deformation of the interface. Hence, it advances at a speed that always exceeds the critical speed needed to form a Landau–Levich film. During this process, the contact lines recede as the film is formed, until the drop detaches from the solid. Fig. 7b shows the cross-over time, t^*, as a function of the initial position of the droplet, x_0, which we use as a measure of the initial deformation of the interface. For the three data sets, t^* decreases with decreasing x_0, at a rate that depends on the droplet volume. We expect that the cross-over time is affected by the timescale of motion of the contact line, t_{cl}, but also by the timescale of translation due to the deformation of the interface. The timescale of motion of the contact line can be written as $t_{cl} \sim R/v_{cap}$, where $R \sim V^{1/3}$ is the base radius of the droplet and $v_{cap} = \gamma/\mu$ is the capillary speed; hence, $t_{cl} \sim \mu V^{\frac{1}{3}}/\gamma$. On the other hand, the deformation of the interface can be characterized by the dimensionless parameter $\Delta r = (x_e - x_0)\beta/V^{1/3}$, which measures deviations of the droplet radius from equilibrium. In terms of these variables, we expect that the cross-over time obeys $t^* \sim t_{cl} f(\Delta r)$ where f is a function determined by the details of the flow pattern. The rescaled data is presented in the inset of Fig. 7b; the data show a reasonable collapse, albeit with deviations for the smaller droplet volume considered, for which we observe longer cross-over times. A possible reason for this deviation is the presence of entrapped oil droplets between the larger droplets and the solid, which increase their mobility and lead to shorter cross-over times.

Conclusions

We have studied the transport of water droplets surrounded by an ambient oil phase in a channel geometry driven by electrowetting, and the subsequent relaxation process once the electrowetting actuation is removed. Experimentally, we have used a wedge geometry as a means to study the directed transport of the droplet. Upon electrowetting actuation, the droplet undergoes a translation towards the apex of the wedge, following two subsequent exponential relaxations of different characteristic timescales. At first, the droplet has a relatively high mobility, indicating that it glides over a lubricating oil film. This is followed by a low-mobility regime, indicating that the film ruptures to form contact lines that slow the droplet down. Once a droplet equilibrates to the configuration imposed by electrowetting, removing the applied voltage leads to outwards motion, where the droplet also follows two subsequent exponential translations to its original equilibrium position. Initially, the drop has a relatively low mobility due to the presence of a dewetting front. This is followed by a regime of higher mobility, indicating the detachment of the liquid–liquid interface from the channel walls. In all cases, however, the dependence of the corresponding characteristic timescale on droplet volume and wedge angle is in agreement with the theory of Ruiz-Gutiérrez *et al.*[22]

We have studied the onset of film breakup during inwards motion in terms of the stability of the entrapped thin film. Using lattice-Boltzmann simulations, we have identified a similar mechanism to the electrowetting-driven destabilization of a Landau–Levich film studied by Staicu and Mugele.[9] However, in the present case of a droplet in confinement, the speed of the interface is not only set by the interplay between the driving electrowetting potential and the resistance of the Landau–Levich film, but also by the constraints imposed by the channel.

A similar situation arises during the relaxation of the droplet upon removal of the electrowetting potential. On the one hand, the timescale of dewetting from the walls is controlled by the speed of the contact line and the initial length scale covered by the drop. On the other, the translation of the droplet is affected by the channel geometry on the droplet's volume. Hence, we propose a scaling of the cross-over time to droplet detachment, which captures the experimental data well.

Hence, the mobility of droplets during electrowetting-dewetting in channel geometries is controlled by the interplay between the intrinsic timescales arising from the fluid flow at small scales, *e.g.*, film entrapment and contact-line motion, and the timescale of the large-scale flow, which depends on the details of the channel geometry. Here we have studied the relatively simple geometry of a wedge channel as a model example. However, we expect that similar competing mechanisms controlling drop mobilities across length scales are present in more complicated channel geometries used, for example, in microfluidic platforms or in oil-recovery technologies.

Conflicts of interest

There are no conflicts to declare.

Acknowledgements

É. R.-G. and R. L.-A. acknowledge financial support from the UK's Engineering and Physical Sciences Research Council (Grant No. EP/R036837/1) and through membership of the UK Consortium on Mesoscale Engineering Sciences (Grant No. EP/R029598/1). D. B. and F. M. acknowledge financial support from the Dutch national Science Foundation NWO (Grant No. 11380 within the VICI program).

References

1 F. Mugele and J. Heikenfeld, *Electrowetting: Fundamental Principles and Practical Applications*, Wiley-VCH, Weinheim, Germany, 2018.
2 F. Mugele and J.-C. Baret, *J. Phys.: Condens. Matter*, 2005, **17**, R705–R774.
3 R. Shamai, D. Andelman, B. Berge and R. Hayes, *Soft Matter*, 2007, **4**, 38–45.
4 B. Berge and J. Peseux, *Eur. Phys. J. E: Soft Matter Biol. Phys.*, 2000, **3**, 159–163.
5 R. A. Hayes and B. J. Feenstra, *Nature*, 2003, **425**, 383–385.
6 M. G. Pollack, R. B. Fair and A. D. Shenderov, *Appl. Phys. Lett.*, 2000, **77**, 1725–1726.
7 M. G. Pollack, A. D. Shenderov and R. B. Fair, *Lab Chip*, 2002, **2**, 96–101.
8 R. de Ruiter, A. M. Pit, V. M. de Oliveira, M. H. G. Duits, D. van den Ende and F. Mugele, *Lab Chip*, 2014, **14**, 883–891.
9 A. Staicu and F. Mugele, *Phys. Rev. Lett.*, 2006, **97**, 167801.
10 J. Gao, N. Mendel, R. Dey, D. Baratian and F. Mugele, *Appl. Phys. Lett.*, 2018, **112**, 203703.
11 R. de Ruiter, C. Semprebon, M. Van Gorcum, M. H. G. Duits, M. Brinkmann and F. Mugele, *Phys. Rev. Lett.*, 2015, **114**, 234501.
12 R. Dangla, S. C. Kayi and C. N. Baroud, *Proc. Natl. Acad. Sci. U. S. A.*, 2013, **110**, 853–858.
13 J. Bico and D. Quéré, *J. Fluid Mech.*, 2002, **467**, 101–127.
14 C. Luo, X. Heng and M. Xiang, *Langmuir*, 2014, **30**, 8373–8380.
15 E. Reyssat, *J. Fluid Mech.*, 2014, **748**, 641–662.
16 J. Hong, J. K. Park, B. Koo, K. H. Kang and Y. K. Suh, *Sens. Actuators, B*, 2013, **188**, 637–643.
17 M. Prakash, D. Quéré and J. W. M. Bush, *Science*, 2008, **320**, 931–934.
18 É. Ruiz-Gutiérrez, J. H. Guan, B. Xu, G. McHale, G. G. Wells and R. Ledesma-Aguilar, *Phys. Rev. Lett.*, 2017, **118**, 218003.
19 D. Baratian, A. Cavalli, D. van den Ende and F. Mugele, *Soft Matter*, 2015, **11**, 7717–7721.
20 É. Ruiz-Gutiérrez and R. A. Ledesma-Aguilar, *Langmuir*, 2019, **35**, 4849–4859.
21 B. Bera, PhD thesis, University of Twente, 2016.
22 É. Ruiz-Gutiérrez, C. Semprebon, G. McHale and R. Ledesma-Aguilar, *J. Fluid Mech.*, 2018, **842**, 26–57.
23 Z. Wang, D. V. D. Ende, A. Pit, R. Lagraauw, D. Wijnperlé and F. Mugele, *Soft Matter*, 2017, **13**, 4856–4863.